ACSNANO

www.acsnano.org

ARTICLE

3D $Ti_3C_2T_x$ MXene–Matrigel with Electroacoustic Stimulation to Promote the Growth of Spiral Ganglion Neurons

Menghui Liao, Yangnan Hu, Yuhua Zhang, Kaichen Wang, Qiaojun Fang, Yanru Qi, Yingbo Shen, Hong Cheng, Xiaolong Fu, Mingliang Tang,* Shan Sun,* Xia Gao,* and Renjie Chai*

Cite This: *ACS Nano* 2022, 16, 16744–16756

Read Online

ACCESS | Metrics & More | Article Recommendations | Supporting Information

ABSTRACT: **Cochlear implantation has become the most effective treatment method for patients with profound and total hearing loss. However, its therapeutic efficacy is dependent on the number and normal physiological function of cochlear implant-targeted spiral ganglion neurons (SGNs). Electrical stimulation can be used as an effective cue to regulate the morphology and function of excitatory cells. Therefore, it is important to develop an efficient cochlear implant electroacoustic stimulation (EAS) system to study the behavior of SGNs. In this work, we present an electrical stimulation system constructed by combining a cochlear implant and a conductive $Ti_3C_2T_x$ MXene–matrigel hydrogel. SGNs were cultured in the $Ti_3C_2T_x$ MXene–matrigel hydrogel and exposed to electrical stimulation transduced by the cochlear implant. It was demonstrated that low-frequency stimulation promoted the growth cone development and neurite outgrowth of SGNs as well as signal transmission between cells. This work may have potential value for the clinical application of the $Ti_3C_2T_x$ MXene hydrogel to optimize the postoperative listening effect of cochlear implantation and benefit people with sensorineural hearing loss.**

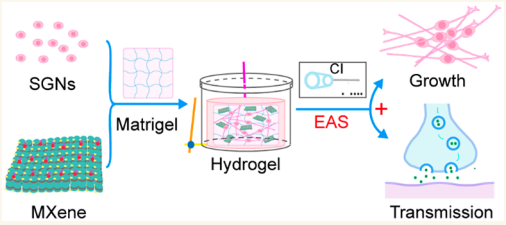

KEYWORDS: *spiral ganglion neuron, $Ti_3C_2T_x$ MXene, hydrogel, cochlear implant, electroacoustic stimulation*

INTRODUCTION

At present, there are about 466 million deaf people in the world, accounting for one-third of the disabled population. Due to the aging of the population, the abuse of ototoxic drugs, noise, and other factors, the number of deaf people is increasing year by year. In the development process through continuous optimization and improvement, cochlear implantation has become the main therapeutic method for the patients with serious and total sensorineural hearing loss.[1] A cochlear implant (CI) can emit special square-wave bidirectional pulses that encode complex multiband speech information and convert it into electrical signals for precise transmission to spiral ganglion neurons (SGNs). Partial hearing is mainly obtained by chronic electrical stimulation of residual spiral ganglion neurons with cochlear implants.[2,3] The insufficient number and dysfunction of residual SGNs are the most important factors that limit the effects of CI and are also the main factors that determine hearing recovery after CI use.[4,5] It is currently believed that the restoration of hearing through self-healing is nearly impossible in mammals with sensorineural deafness. The fundamental reason is that the repair capacity of adult mammalian hair cells (HCs) and SGNs after injury is very limited.[6,7] Even if some regenerated inner ear HCs could be obtained,[8] the neurites of SGNs would need to to grow and distribute onto HCs for hearing loss repair to actually be possible. In order to expand the indications of CI, the regulation of the survival, regeneration, morphology, and function of SGNs is one of the major medical problems that urgently needs to be solved.

Electrical activity is involved in many aspects of early neuronal development,[9] implying that electrical stimulation can manipulate the morphology and function of excitatory cells, such as in nerve regeneration.[10,11] Intracochlear chronic electrical stimulation has been extensively studied to reduce the degeneration of neurons.[12] Studies have indicated that axonal regeneration and muscle reinnervation could be accelerated by low-frequency bidirectional postoperative electrical stimulation in carpal tunnel syndrome patients.[13] In addition, direct current stimulation and chronic low-frequency

Received: June 27, 2022
Accepted: October 10, 2022
Published: October 12, 2022

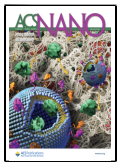

https://doi.org/10.1021/acsnano.2c06306
ACS Nano 2022, 16, 16744–16756

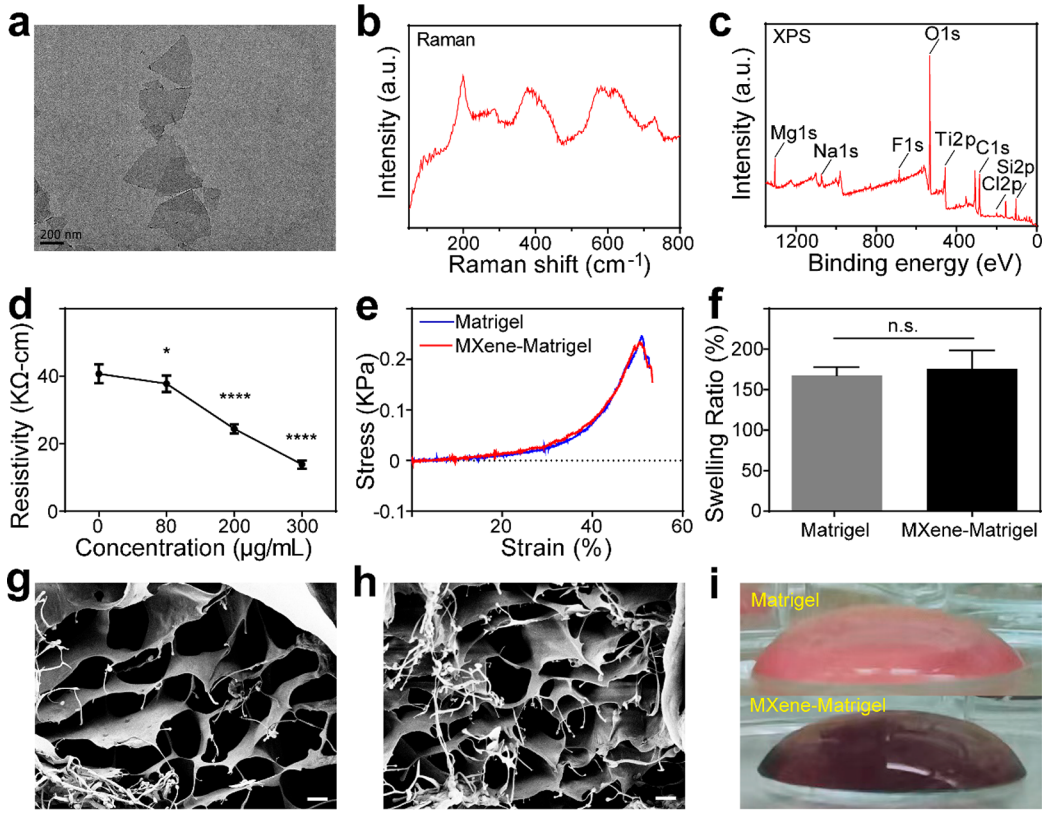

Figure 1. Characterization of $Ti_3C_2T_x$ MXene and the $Ti_3C_2T_x$ MXene−matrigel hydrogels. (a) High-resolution TEM image of $Ti_3C_2T_x$ MXene nanosheets. Scale bar represents 200 nm. (b) Raman spectrum of $Ti_3C_2T_x$ MXene. (c) XPS pattern of $Ti_3C_2T_x$ MXene. (d) Resistivity of $Ti_3C_2T_x$ MXene−matrigel hydrogels with different concentrations. (e) Mechanical stress test results of the matrigel hydrogel and the $Ti_3C_2T_x$ MXene−matrigel hydrogel. (f) Equilibrium swelling ratio of the matrigel hydrogel and the $Ti_3C_2T_x$ MXene−matrigel hydrogel. (g) SEM image of the matrigel hydrogel. Scale bar represents 20 μm. (h) SEM image of the $Ti_3C_2T_x$ MXene−matrigel hydrogel. Scale bar represents 20 μm. (i) Side view of the matrigel hydrogel (top) and the $Ti_3C_2T_x$ MXene−matrigel hydrogel at a concentration of 80 μg/mL (bottom). Data are presented as mean ± SD (*P < 0.05, ****P < 0.0001; and n.s. is P > 0.05, no significant difference).

electrical stimulation can modulate the excitability, neural network maturation, and synchronization of neurons *in vitro*.[14] Shen et al. found that charge-balanced bidirectional electrical stimulation significantly reduced the length of neurites in SGNs when the intensity more than 50 μA or the stimulation lasted longer than 8 h.[15] However, the results of these studies were unsatisfactory. This may be due to the fact that the regulation of various cellular behaviors by electrical stimulation depends on cell type, cell state, and parameters of electrical stimulation.[16,17] These studies not only illustrate the importance of electrical stimulation in reducing SGN degeneration but also demonstrate that simple electrical stimulation cannot regenerate the SGNs. Therefore, it is necessary to develop an efficient cochlear implant electro-acoustic stimulation (EAS) system and study its regulation of the behavior of SGNs.

Recent advances in materials and technologies have brought opportunities for regulating the growth of SGNs. The interaction between materials and cells can be converted into biological signals,[18] triggering a series of intracellular cascade reactions[19] that ultimately lead to changes in cell behavior. The development of suitable biomaterials is conducive to the clinical application of SGNs, which will greatly improve the listening effect after cochlear implantation. Nanomaterials show great application potential in the fields of biomedicine and tissue engineering. MXenes are late models of 2D nanostructures.[20] They have a "Mn + 1Xn" sandwich structure, where M is a transition-metal element[21] and X is a carbon element or nitrogen element.[22] MXenes not only have the conductivity of transition metals,[23] but also have the hydrophilicity of surface functional groups.[24,25] They can be flexibly functionalized through different surface modifications. Because of their great hydrophilicity and biocompatibility,[26] MXenes have broad application prospects in the biomedical field, such as electrochemical biosensing,[27] diagnostic imaging,[28,29] infrared photothermal therapy (PTT),[28] antibacterial preparation,[30,31] drug delivery,[32] and other fields. The latest research found that $Ti_3C_2T_x$ MXene can be used as an excellent neural interface material to facilitate the maturation of neural stem cell (NSC) derived neurons.[33] Therefore, we chose $Ti_3C_2T_x$ MXene nanosheets as the conductive element in the EAS system.

At present, most studies focus on the regulation of 2D substrates on cells, as it is difficult to simulate the 3D environment of cells *in vivo*. To better simulate the *in vivo* biological environment, a 3D *in vitro* culture system was developed and applied in this study. Matrigel is an extract of the Engelbreth−Holm−Swarm (EHS) tumor mainly composed of laminin-111. It can simulate the structure, composition, physical characteristics, and function of the cell basement membrane *in vivo*, which is conducive to *in vitro* cell cultures.[34] At high concentrations (greater than 4 mg/mL), a gel formed at 24−37 °C. BME−matrigel is widely used in tissue and cell transplantation studies, including stem cells, and

https://doi.org/10.1021/acsnano.2c06306
ACS Nano 2022, 16, 16744−16756

higher survival and tissue regeneration rates were observed.[35] Therefore, we constructed a 3D culture system by incorporating $Ti_3C_2T_x$ MXene nanosheets into a matrigel hydrogel ($Ti_3C_2T_x$ MXene−matrigel) and investigated the regulation of the system on cells. Moreover, we further established cochlear implant electroacoustic stimulation (EAS) system based on the $Ti_3C_2T_x$ MXene−matrigel and explored the development of mouse SGNs and its regulation of the neural network formation and performance *in vitro*. This work has the potential to optimize the postoperative listening effect of cochlear implantation and benefit people with sensorineural hearing loss.

RESULTS AND DISCUSSION

Successful Preparation of $Ti_3C_2T_x$ MXene and the $Ti_3C_2T_x$ MXene Hydrogel. We synthesized $Ti_3C_2T_x$ MXene solution by chemically etching the Al atomic layer in Ti_3AlC_2 in a mixture of HCl and LiF. Raman spectroscopy, X-ray photoelectron spectroscopy (XPS), and transmission electron microscopy (TEM) were used to verify the successful preparation of the $Ti_3C_2T_x$ MXene. It could be observed from the TEM image that the prepared $Ti_3C_2T_x$ MXene displayed a monolayer nanosheet structure with lateral sizes in the range of several hundred nanometers (Figure 1a). It could be seen from the Raman spectrum (Figure 1b) that $Ti_3C_2T_x$ had various characteristic peaks in the range of 100−800 cm^{-1}. The region between 230 and 470 cm^{-1} represented the vibrations of surface groups attached to titanium atoms, which influenced by the surface atoms. The 580−730 cm^{-1} region was mainly attributed to carbon vibrations. The full XPS spectrum also presented a typical $Ti_3C_2T_x$ MXene pattern (Figure 1c), showing that $Ti_3C_2T_x$ MXene was mainly composed of Ti, C, and O. The above results suggested that we had successfully prepared $Ti_3C_2T_x$ MXene. Subsequently, we evaluated the stability of $Ti_3C_2T_x$ MXene by comparing the changes in compositional elements and the absorbance of the $Ti_3C_2T_x$ MXene solution over time (Supplementary Figure 1). The scanning electron microscopy (SEM)−energy-dispersive X-ray spectroscopy (EDX) results showed that the Ti element content in $Ti_3C_2T_x$ MXene gradually decreased with time while the O element content gradually increased (Supplementary Figure 1a), indicating that the $Ti_3C_2T_x$ MXene oxidized slowly with time. The absorbance changes were quantified by fitting the data to the function $f(x) = y_0 + Ae^{-x/\tau}$, where τ is the time constant, A is the amplitude, and y_0 is the offset value.[36] The results showed that the τ of $Ti_3C_2T_x$ MXene stored at low temperature (LT) (17.5 days) was larger than that of $Ti_3C_2T_x$ MXene stored at room temperature (RT) (11.2 days) (Supplementary Figure 1b and c). After 30 days of storage, the $Ti_3C_2T_x$ MXene stored at LT was significantly darker than that stored at RT (Supplementary Figure 1b). These results suggested that the stability of $Ti_3C_2T_x$ MXene decreased gradually with time and was significantly improved by storage in a LT environment.

2D $Ti_3C_2T_x$ MXene was used in our previous work. In order to better simulate the microenvironment *in vivo*, it is necessary to establish a conductive 3D culture system based on $Ti_3C_2T_x$ MXene. Next, we constructed $Ti_3C_2T_x$ MXene−matrigel hydrogels by incorporating different concentrations of the $Ti_3C_2T_x$ Mxene solution into the matrigel. The electrical conductivity of $Ti_3C_2T_x$ MXene−matrigel hydrogels with different concentrations was then evaluated by resistivity tests. Compared with the pure matrigel (40.7 ± 2.78 KΩ-cm), the $Ti_3C_2T_x$ MXene−matrigel hydrogels had lower resistivities. As the $Ti_3C_2T_x$ MXene concentration increased, the resistivity became smaller and smaller (80 μg/mL, 37.8 ± 2.43 KΩ cm; 200 μg/mL, 24.4 ± 1.36 KΩ cm; and 300 μg/mL, 13.9 ± 1.20 KΩ-cm; Figure 1d), indicating that the incorporation of $Ti_3C_2T_x$ MXene enhanced the conductivity of the matrigel hydrogel. The mechanical properties of the matrigel hydrogel and the $Ti_3C_2T_x$ MXene−matrigel hydrogel were assessed. It was demonstrated that the incorporation of $Ti_3C_2T_x$ MXene did not change the mechanical stress of the matrigel hydrogel (Figure 1e). The cross-linking index of the material was measured by the equilibrium swelling ratio. There was no significant difference between the hydrogels (168 ± 9.85% for the matrigel vs 176 ± 22.7% for $Ti_3C_2T_x$ MXene−matrigel , p = 0.5992, Figure 1f). To observe the surface ultrastructure of the matrigel and the $Ti_3C_2T_x$ MXene−matrigel hydrogel, we performed SEM imaging. As shown in Figure 1g and h, there was no obvious difference in structure between the two hydrogels; both had large pores, which are conducive to cell adhesion and growth. We further detected the elemental composition of the matrigel and $Ti_3C_2T_x$ MXene−matrigel using SEM-EDX spectra to prove the incorporation of $Ti_3C_2T_x$ MXene into the matrigel (Supplementary Figure 2). The results showed that signals of the main elements of $Ti_3C_2T_x$ MXene such as Ti and F were not detected in the matrigel hydrogel analysis area (Supplementary Figure 2a) but were detected in the $Ti_3C_2T_x$ MXene−matrigel hydrogel analysis area (Supplementary Figure 2b), suggesting the successful incorporation of $Ti_3C_2T_x$ MXene into the matrigel. In addition, the cavity diameter of the hydrogel did not change after $Ti_3C_2T_x$ MXene was integrated into the matrigel (17.22 ± 6.07 μm for the matrigel vs 18.25 ± 5.97 μm for $Ti_3C_2T_x$ MXene−matrigel, p = 0.0992; Supplementary Figure 2 c and d). Figure 1i shows the side views of the matrigel and $Ti_3C_2T_x$ MXene−matrigel hydrogel. It can be observed that the the hydrogel turned black after the addition of $Ti_3C_2T_x$ MXene.

$Ti_3C_2T_x$ MXene−Matrigel Hydrogels Exhibit Great Biocompatibility. The cytotoxicity of a material determines its application in the biomedical field. Therefore, we examined the biocompatibilities of a pure matrigel hydrogel (0 μg/mL) and $Ti_3C_2T_x$ MXene−matrigel hydrogels with SGNs at concentrations of 40, 80, 100, 200, and 300 μg/mL. Live and dead cells were labeled with Calcein-AM and EthD-1, respectively. Immunofluorescence images showed that the vast majority of SGNs were living cells after three days of culture in $Ti_3C_2T_x$ MXene hydrogels (Supplementary Figure 3a). More than 98% of the cells were Calcein-AM positive, and different concentrations of $Ti_3C_2T_x$ MXene hydrogels had no obvious effect on the survival of SGNs (Supplementary Figure 3b). In addition, we used the WST-8-based cell counting kit-8 (CCK-8) cytotoxicity assay to examine the cytotoxicities of different concentrations of $Ti_3C_2T_x$ MXene−matrigel hydrogels to SGNs from day 3 to day 9 (Supplementary Figure 3c). The results showed that there was no obvious difference in cell viability with the increase of $Ti_3C_2T_x$ MXene concentration, indicating that the $Ti_3C_2T_x$ MXene−matrigel hydrogels had little cytotoxicity to SGN. We also observed the morphology of SGNs cultured in $Ti_3C_2T_x$ MXene hydrogel by SEM, as shown in Supplementary Figure 3d. SEM images suggested that the SGNs had a normal cell morphology in the $Ti_3C_2T_x$ MXene hydrogel. SGNs cultured in $Ti_3C_2T_x$ MXene hydrogels with different concentrations were as viable as those cultured in the pure matrigel hydrogel and even exhibited better neurite

https://doi.org/10.1021/acsnano.2c06306
ACS Nano 2022, 16, 16744−16756

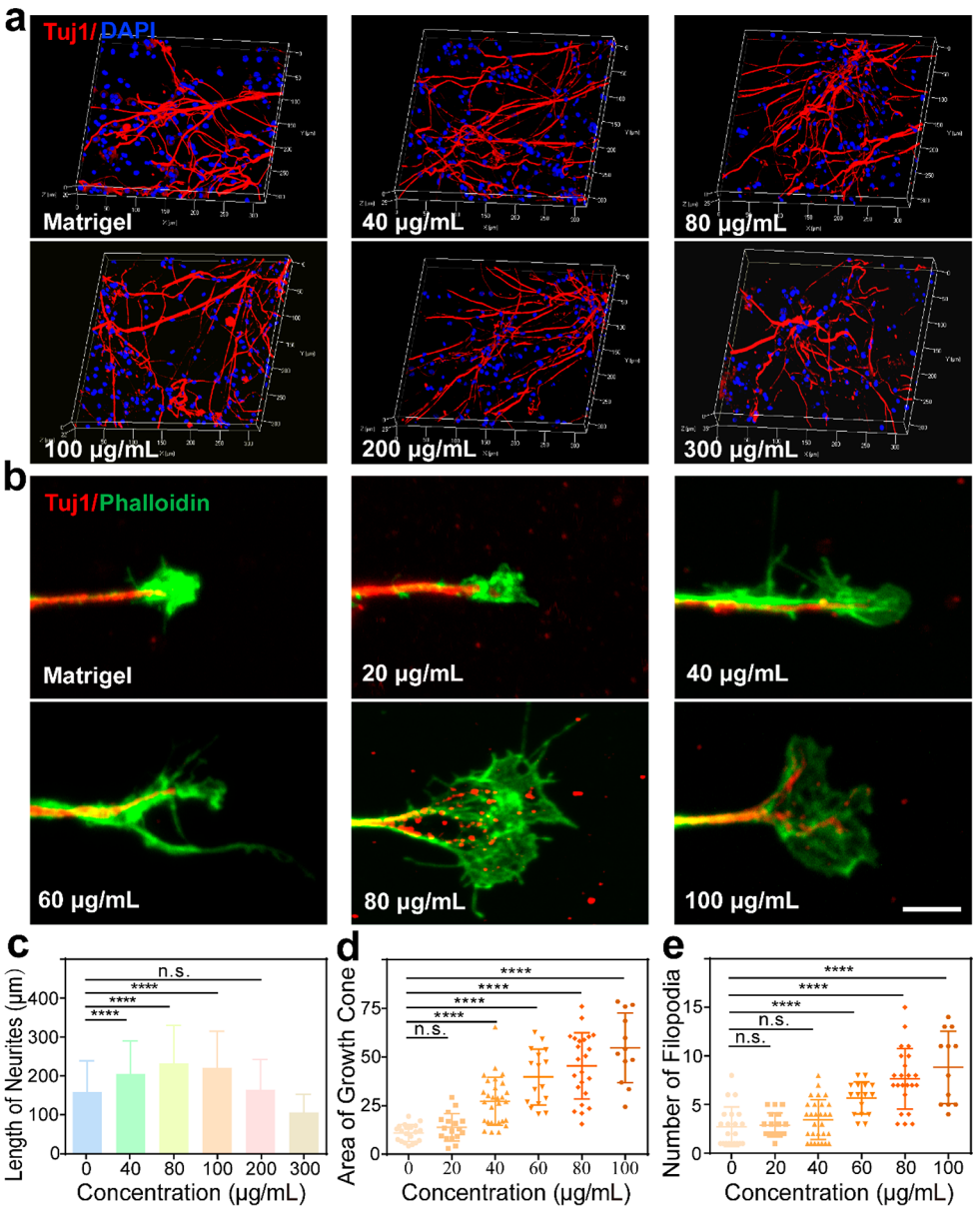

Figure 2. The $Ti_3C_2T_x$ MXene–matrigel hydrogel promoted the growth of SGNs *in vitro*. (a) Representative immunofluorescence 3D images of SGNs after seven days of culture in hydrogels with different concentrations of $Ti_3C_2T_x$ MXene. SGNs were labeled with Tuj1 (red), and nuclei were labeled with DAPI (blue). (b) Representative immunofluorescence images of growth cones of SGNs after three days of culture in hydrogels with different concentrations of $Ti_3C_2T_x$ MXene. SGNs were labeled with Tuj1 (red), and growth cones were labeled with phalloidin (green). Scale bar represents 5 μm. (c) Statistics of the neurite length of cultured SGNs in the experiment shown in panel a. (d) Statistics of the growth cone area of the cultured SGNs in the experiment shown in panel b. The unit of the ordinate is micrometers squared (μm^2). (e) Number of growth cone filopodia of cultured SGNs in the experiment shown in panel b. Data are presented as mean ± SD (n.s. is $P > 0.05$, ****$P < 0.0001$).

growth. The above results indicate that the $Ti_3C_2T_x$ MXene–matrigel hydrogel exhibits great cytocompatibility and is an excellent interface material for SGNs.

The $Ti_3C_2T_x$ MXene–Matrigel Hydrogel Regulates the Growth of SGNs *In Vitro*. The core of tissue engineering is to explore the regulation of cell behavior by the physical and chemical properties of biomaterials.[37] Therefore, we investigated the regulation effects of conductive hydrogels with different concentrations (40, 80, 100, 200, and 300 μg/mL) of $Ti_3C_2T_x$ MXene on SGNs compared with the pure matrigel hydrogel (0 μg/mL). The results showed that SGNs grew well at all concentrations after seven days of culture (Figure 2a). In addition, the neurite length of the SGNs showed that $Ti_3C_2T_x$ MXene hydrogels at concentrations of 40–100 μg/mL significantly promoted the outgrowth of neurites (0 μg/mL, 159 ± 80.3 μm; 40 μg/mL, 205 ± 84.7 μm; 80 μg/mL, 232 ± 98.4 μm; 100 μg/mL, 221 ± 93.7 μm; 200 μg/mL, 164 ± 79.0 μm; and 300 μg/mL, 106 ± 46.2 μm, Figure 2b). In order to further determine which concentration was more suitable for the growth of SGNs, we cultured SGNs with $Ti_3C_2T_x$ MXene hydrogels at different concentrations and investigated the development of growth cones. The growth cones, special structures composed of actin at the neurite terminal, can respond to intracellular signals and sense changes in the external environment. We analyzed multiple morphological indicators of the growth cones, including growth cone area,

https://doi.org/10.1021/acsnano.2c06306
ACS Nano 2022, 16, 16744–16756

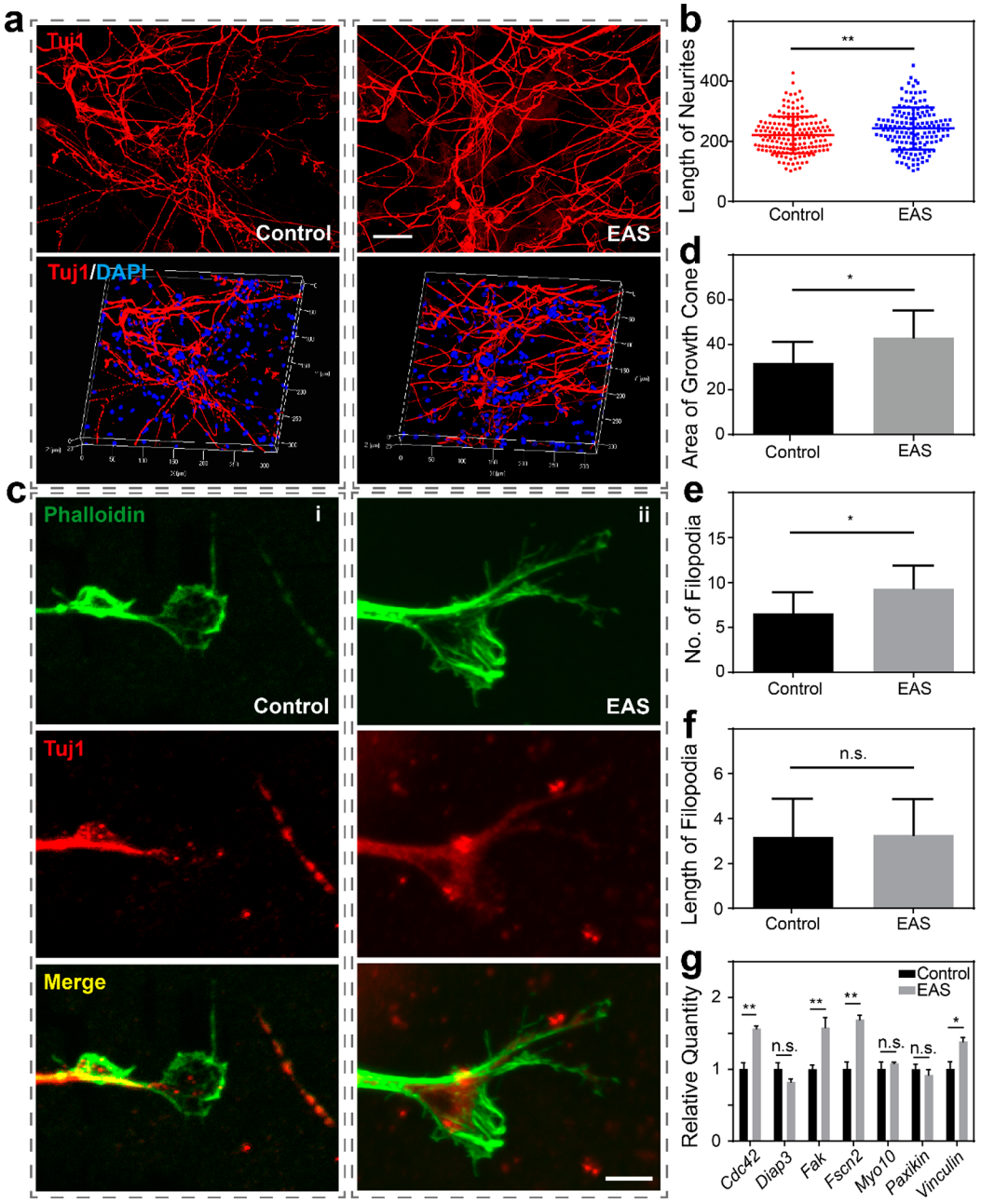

Figure 3. The cochlear implant−$Ti_3C_2T_x$ MXene−matrigel hydrogel−EAS system promoted the growth of SGNs. (a) Representative immunofluorescence images of SGNs cultured in the $Ti_3C_2T_x$ MXene hydrogel (left) and the cochlear implant−$Ti_3C_2T_x$ MXene−matrigel hydrogel−EAS system (right). Scale bar represents 40 μm. The top panels are the front-view images, and the bottom panels are the 3D reconstruction images. SGNs were labeled with Tuj1 (red), and nuclei were labeled with DAPI (blue). (b) Average neurite lengths of SGNs in the control and EAS groups. The unit of the ordinate is micrometers (μm). (c) Immunofluorescence images of SGN growth cones in the $Ti_3C_2T_x$ MXene hydrogel with our without EAS for (i) the control group and (ii) the EAS group. Growth cones were labeled with phalloidin (green), and SGNs were labeled with Tuj1 (red). Scale bar represents 5 μm. (d) Statistical graph of the growth cone area. The unit of the ordinate is micrometers squared (μm^2). (e) Statistical graph of the number of filopodia. (f) Statistical graph of the filopodia length. The unit of the ordinate is micrometers (μm). (g) mRNA expression levels of relevant adhesion molecules. Data are presented as mean ± SD (*P < 0.05, **P < 0.01).

filopodia number, and filopodia length. As the $Ti_3C_2T_x$ MXene hydrogel concentration increased, the growth cone area of SGNs gradually increased (0 μg/mL, 11.0 ± 4.36 μm^2; 20 μg/mL, 13.8 ± 7.05 μm^2; 40 μg/mL, 27.3 ± 12.3 μm^2; 60 μg/mL, 39.7 ± 14.4 μm^2; 80 μg/mL, 45.5 ± 17.0 μm^2; and 100 μg/mL, 54.7 ± 17.9 μm^2; Figure 2c), exhibiting a significant difference from 40 to 100 μg/mL. When the concentration was increased to 60−100 μg/mL, the filopodia number of SGNs increased gradually and significantly (0 μg/mL, 2.71 ± 2.03; 20 μg/mL, 2.89 ± 1.23; 40 μg/mL, 3.45 ± 2.05; 60 μg/mL, 5.69 ± 1.66; 80 μg/mL, 7.65 ± 3.13; and 100 μg/mL, 8.83 ± 3.71; Figure 2d). What's more, increasing the $Ti_3C_2T_x$ MXene concentration in the hydrogel had no significant effect on the filopodia length of cultured SGNs (data not shown). There was no significantly difference in the three parameters of the growth cones and the neurite length of SGNs between 80 and

https://doi.org/10.1021/acsnano.2c06306
ACS Nano 2022, 16, 16744−16756

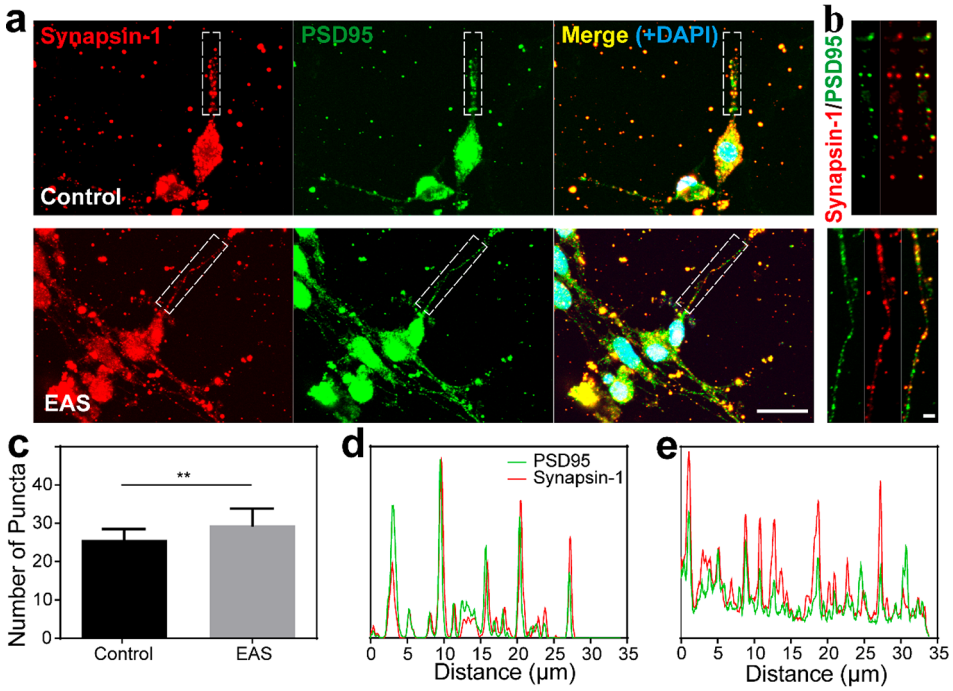

Figure 4. Effect of EAS on the synaptic development of SGNs cultured in the $Ti_3C_2T_x$ MXene hydrogel. (a) Representative low-magnification image of SGN synaptic staining after 14 days of culture in the $Ti_3C_2T_x$ MXene hydrogel with or without EAS. Scale bar represents 20 μm. Synapsin-1 was used as a marker for presynapsin (red), PSD95 was used as a marker for postsynapsin (green), DAPI was used to label the nucleus (blue). (b) High-magnification view of the synapse in the area of the white dotted box in panel a (control group, top; EAS group, bottom). Scale bar represents 2 μm. (c) Statistical plot of synaptic puncta densities per 50 μm where synapsin-1 and PSD95 overlapped. (d) Tracking map of the fluorescence intensity corresponding to the control group in panel b. (e) Tracking map of fluorescence intensity corresponding to the EAS group in panel b. Data are presented as mean ± SD (P < 0.01).**

100 μg/mL. Therefore, subsequent experiments adopted a $Ti_3C_2T_x$ MXene hydrogel with a concentration of 80 μg/mL.

Cochlear Implant–$Ti_3C_2T_x$ MXene–matrigel Hydrogel Electroacoustic Stimulation System Promotes the Neurite Outgrowth of SGNs. We further prepared an EAS system based on a $Ti_3C_2T_x$ MXene–matrigel hydrogel and CI. In our previous study, we found that high-frequency EAS can cause neurotoxicity, while low-frequency EAS can promote the proliferation and differentiation potential of NSCs.[33,38] Therefore, in this study, we mainly explored the effects of low-frequency EAS on SGNs. To evaluate the biocompatibility of the cochlear implant–$Ti_3C_2T_x$ MXene–matrigel hydrogel–EAS system, we performed EAS on SGNs for seven days, with continuous low-frequency stimulation for 10 min every day. The morphologies of the SGNs in both the control ($Ti_3C_2T_x$ MXene–matrigel hydrogel without EAS) and EAS ($Ti_3C_2T_x$ MXene–matrigel hydrogel with EAS) groups were normal, but SGNs with the EAS treatment seemed to grow better with longer neurites (222 ± 60.9 μm for the control group vs 243 ± 70.0 μm for the EAS group, p = 0.0033; Figure 3a and b). Combined with the biocompatibility results (Supplementary Figure 3), the results illustrated that this system was not neurotoxic to SGNs. These results suggested that the cochlear implant–$Ti_3C_2T_x$ MXene–matrigel hydrogel–EAS system was cytocompatible and could be used to study the regulation of the behavior of SGNs *in vitro*.

In order to explore how the cochlear implant–$Ti_3C_2T_x$ MXene–matrigel hydrogel–EAS system regulated the neurite development of SGNs, we focused on the development of growth cones (Figure 3c). We performed cochlear implant-based EAS on SGNs cultured in the $Ti_3C_2T_x$ MXene hydrogel for three days, with continuous stimulation for 10 min per day. The area of the growth cone and the length and number of the filopodia were statistically analyzed. Compared with control, both the area of the growth cone (32.0 ± 9.26 μm^2 for the control group vs 43.2 ± 12.1 μm^2 for the EAS group, p = 0.0206; Figure 3d) and the number of filopodia (6.56 ± 2.35 for the control group vs 9.33 ± 2.55 for the EAS group, p = 0.0288; Figure 3e) significantly increased after EAS. There was no significant difference in the length of filopodia between the two groups (3.18 ± 1.70 μm for the control group vs 3.27 ± 1.59 μm for the EAS group, p = 0.7217; Figure 3f). Since cell adhesion is closely related to the maintenance of cell expansion and function,[39] we detected the mRNA expression levels of seven related genes, namely, *Cdc42*, *Diap3*, *Fak*, *Fscn2*, *myosin-10*, *paxikin* and *vinculin*, using RT-qPCR (Figure 3g). It was found that the expression levels of *Cdc42*, *Fak*, *myosin-10*, and *vinculin* increased significantly after the cochlear implant–$Ti_3C_2T_x$ MXene–matrigel hydrogel EAS. After the cochlear implant EAS, SGNs cultured in the $Ti_3C_2T_x$ MXene–matrigel hydrogel had longer neurites and larger growth cone areas and filopodia. These results indicated that EAS has a positive regulatory effect on the growth of SNGs in the $Ti_3C_2T_x$ MXene hydrogel.

The Cochlear Implant–$Ti_3C_2T_x$ MXene–matrigel Hydrogel EAS System Promotes the Formation of Neural Networks. Synapsin-1 and postsynaptic density protein 95 (PSD95) have been shown to be closely related to synaptic maturation and synaptic plasticity.[40] To explore whether the SGNs cultured in the $Ti_3C_2T_x$ MXene hydrogel were mature, we used immunofluorescence staining to detect the synaptic density of neurons cultured for 14 days. The SGNs in both the

https://doi.org/10.1021/acsnano.2c06306
ACS Nano 2022, 16, 16744–16756

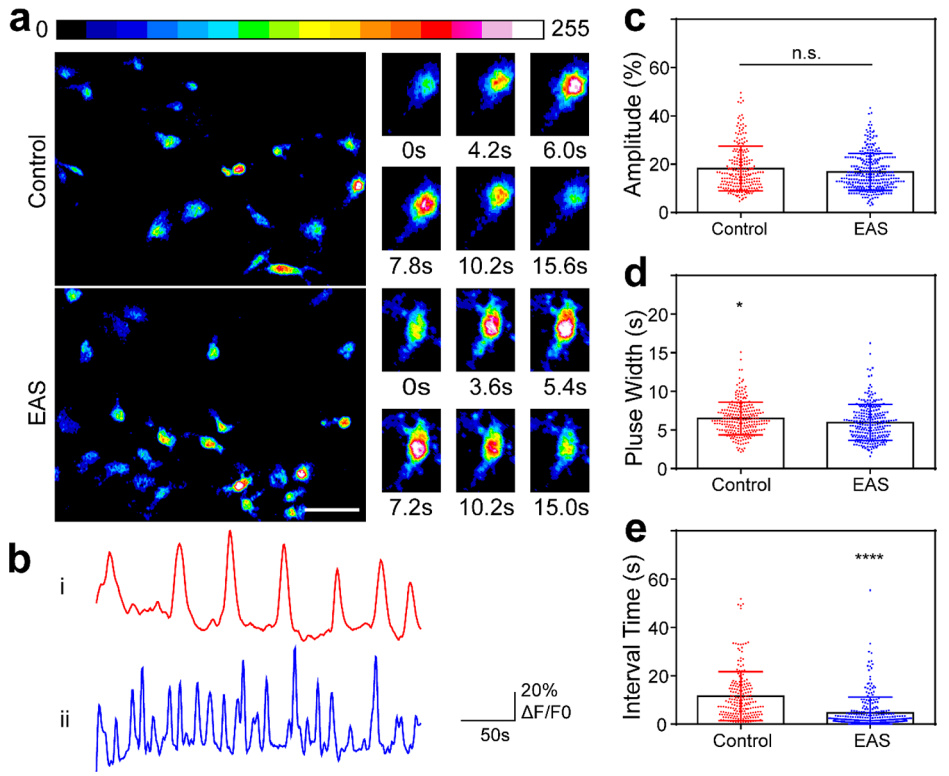

Figure 5. $Ti_3C_2T_x$ MXene−matrigel hydrogel−EAS system affected calcium oscillations of mice SGNs *in vitro*. (a) Representative image of transient Ca^{2+} changes during calcium oscillations in SGNs. The shade of the color reflects the different intracellular Ca^{2+} concentrations. The six panels on the right side represent the decomposition of the calcium oscillation cycle for a single SGN. Scale bar represents 50 μm. (b) Calcium oscillation tracer waveform of SGNs in (i) the control group and (ii) the EAS group. (c−e) Statistical results showing the amplitude, pulse width, and interval time of calcium oscillations, respectively. Each point represents a calcium oscillation-related parameter of the cells. Data are presented as mean ± SD (*P < 0.05, ****P < 0.0001).

control group and the EAS group formed neural networks, and both synapsin-1 and PSD95 were widely expressed on axons (Figure 4a). An enlarged view of the neuronal synaptic staining showed that both synapsin-1 and PSD95 were speckled and colocalized on axons of SGNs (Figure 4b). The intensities of the synapsin-1 and PSD95 fluorescent spots in the control and EAS groups were traced, and the results demonstrated that these two proteins exhibited strong colocalization signals in both groups (Figure 4d and e, respectively). This suggested that synapses of the SGNs had mature potential, and resulted in normal synaptic structures. The above results indicated that the $Ti_3C_2T_x$ MXene hydrogel EAS system did not influence the expression or colocalization of the two synapse proteins. The number of SGN synapses in the $Ti_3C_2T_x$ MXene−matrigel hydrogel was significantly higher after cochlear implant EAS. (25.6 ± 2.87 for the control group vs 29.5 ± 4.37 for the EAS group, p = 0.0029; Figure 4c). Fluorescence intensity tracing results also showed that there were more synaptic puncta signals in the EAS group (Figure 4d and e). These results highlighted the ability of this system to promote SGN development and maturation. Low-frequency EAS may promote the formation of neural networks, but further experimental verification is required.

SGNs Cultured in the Cochlear Implant−$Ti_3C_2T_x$ MXene Hydrogel−EAS System Produce a Higher Frequency of Calcium Oscillation *In Vitro*. As a second messenger, Ca^{2+} plays an important regulatory role in the development and maturation of SGNs.[41,42] In order to study the effect of the $Ti_3C_2T_x$ MXene hydrogel on calcium oscillations of SGNs, we used the Ca^{2+} fluorescent probe Fluo4-AM to detect the change in Ca^{2+} concentration in SGNs. Figure 5a displays the fluorescence intensity information for SGNs at certain times. The six panels on the right show the calcium oscillation cycle of a single SGN, showing the change of the fluorescence signal from weak to strong and then weak again (Figure 5a, right). From normalized waveforms of calcium oscillations of SGNs on the $Ti_3C_2T_x$ MXene hydrogel with or without EAS (Figure 5b), we could observe that SGNs in both groups had calcium oscillations. The amplitude, pulse width, and the interval between calcium oscillations reflect the relative magnitude, the duration, and the frequency of intracellular calcium oscillations,[43] respectively. Therefore, we quantified these three waveform parameters of calcium oscillations. There was no significant difference in amplitude after EAS (18.2 ± 9.29 for the control group vs 16.8 ± 7.64 for the EAS group, p = 0.0565; Figure 5c), but the shorter pulse width was shorter (6.48 ± 2.11 s for the control group vs 5.98 ± 2.32 s for the EAS group, p = 0.0108; Figure 5d) and the frequency was higher (interval times of 11.5 ± 10.1 s for the control group vs 4.85 ± 6.60 s for the EAS group, p < 0.0001; Figure 5e). These results suggested that EAS resulted in no change in the relative amplitude but led to a shorter duration and higher frequency of calcium oscillations in SGNs in the $Ti_3C_2T_x$ MXene−matrigel hydrogel, implying that the cochlear implant−$Ti_3C_2T_x$ MXene−matrigel hydrogel−EAS system could accelerate the signal transmission induced by Ca^{2+} of SGNs *in vitro*. They may enhance signaling by increasing connections between synapses. The SGNs exhibited

https://doi.org/10.1021/acsnano.2c06306
ACS Nano 2022, 16, 16744−16756

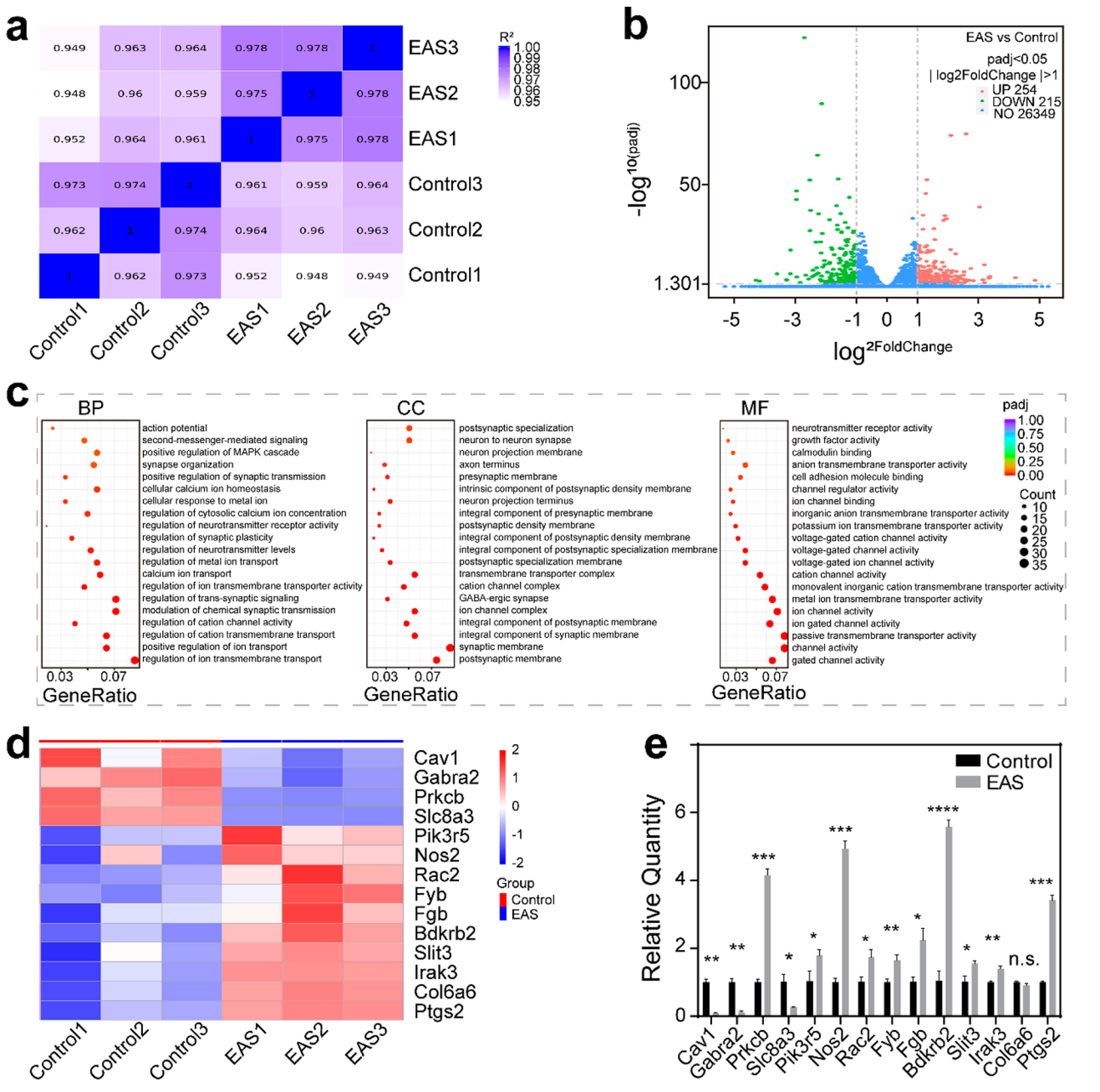

Figure 6. Differential gene analysis of SGNs in the control and EAS groups. (a) Heat map showing the gene expression level correlation between samples. The values were the squares of the correlation coefficients. (b) Volcano plot of differentially expressed genes between the control group and the EAS group. The abscissa represent the change of gene expression multiple between the two groups ($\log^{2FoldChange}$), and the ordinate represents the significance level of the expression difference between the two groups ($-\log^{10PADj}$). $|\log^{2FoldChange}| \geq 1$ and padj$\leq$ 0.05 were the screening standards for differential genes. Up-regulated genes are shown as red dots (right), down-regulated genes are shown as green dots (left), and genes with no difference are shown as blue dots. (c) GO enrichment analysis. The abscissa is the gene ratio, and the ordinate is the 20 enrichment GO terms. The sizes of the dots represent the number of genes enriched, and the color represents the significance of enrichment. (d) Cluster heat maps of differentially expressed genes in the control group and the EAS group. The ordinate is the normalized value of the differential gene FPKM. The colors represent the expression level. (e) mRNA expression levels of genes in the cluster heat map. Data are presented as mean ± SD (*P < 0.05, **P < 0.01, ***P < 0.001, ****P < 0.0001)

a higher frequency of calcium oscillation events in the cochlear implant−$Ti_3C_2T_x$ MXene−matrigel hydrogel−EAS system, which further reflected the role of this system in promoting the formation of neural networks.

Differential Gene Analysis of SGNs. Next, we performed RNA sequencing (RNA-seq) on SGNs in the control and EAS groups. Using the FPKM values of all genes in each sample, the correlation coefficients of samples were calculated and drawn into a heat map (Figure 6a). The results suggested that R^2 between pairs of all samples was ≥0.948, and the correlation coefficient of samples within groups was greater than that between groups, indicating that the similarity of expression patterns among samples was high and the biological repetition was reliable. After the quantification of gene expression was complete, genes with significantly different expression levels were screened. The distribution of the differentially expressed

https://doi.org/10.1021/acsnano.2c06306
ACS Nano 2022, 16, 16744−16756

genes between the control group and the EAS group was visually demonstrated with a volcano plot (Figure 6b). A total of 469 genes were significantly different between the control group and the EAS group, including 254 up-regulated genes and 215 down-regulated genes. This result indicated that the expression of endogenous genes of SGNs during growth was significantly different after EAS. GO function analysis based on differential genes was performed at the three levels of biological process (BP), cell composition (CC), and molecular function (MF) (Figure 6c). The scatter plot showed that 20 GO terms were significantly enriched at each of the three levels. The main BPs were involved in the regulation of ion transmembrane transport, cation channel activity, and synaptic plasticity. The nodes in the directed acyclic graphs (DEGs) were mainly enriched in the postsynaptic membrane, the synaptic membrane, the ion channel complex, and the synapse. The main MFs were related to gated channel activity, passive transmembrane transporter activity, ion channel activity, and cell adhesion molecule binding. The expression levels of 14 related genes were clustered, which indicated that the expression of *Pik3r5*, *Nos2*, *Rac2*, *Fyb*, *Fgb*, *Bdkrb2*, *Slit3*, *Irak3*, *Col6a6*, and *Ptgs2* was up-regulated and the expression of *Cav1*, *Gabra2*, *Prkcb*, and *Slc8a3* was lower in the EAS group (Figure 6d). To further confirm the analyzed data, we verified the mRNA expression levels of these genes by qPCR (Figure 6e). The results showed that the expression of *Cav1*, *Gabra2*, *Slc8a3*, *Pik3r5*, *Nos2*, *Rac2*, *Fyb*, *Fgb*, *Bdkrb2*, *Slit3*, *Irak3*, and *Ptgs2* was consistent with the clustering results. However, the expression of *Prkcb* was up-regulated, while that of *Col6a6* was not significantly different. This inconsistency may be due to the fact that RNA-seq was used for large-scale screening and reflected the overall gene expression trend of the samples, so it could not guarantee that the change trend of each gene was consistent with qPCR. The genes with significant differences between the two groups were significantly enriched in ion transmembrane transport, synaptic transmission, synaptic plasticity, and cell adhesion. Based on the above results, the cochlear implant−$Ti_3C_2T_x$ MXene−matrigel hydrogel−EAS system might affect these related functions of SGNs and thus regulate the neurite growth, maturation, synaptic plasticity, neural network formation, and signal transmission of SGNs.

In future studies, it is necessary to establish animal models of SGN injury and explore the implantation route of $Ti_3C_2T_x$ MXene-based conductive hydrogels and cochlear implants into the inner ear. Further *in vivo* functional validation is required, including the survival and growth of the SGNs, the function of neurons, and hearing restoration in model animals. The coordinated regulation of a conductive hydrogel and specific signaling pathways on SGNs can be further studied to further facilitate the regeneration of SGNs after injury and the recovery of auditory function. If SGNs can be synergistically regulated using the $Ti_3C_2T_x$ MXene−matrigel hydrogel in combination with various signaling pathways, it will be helpful for the clinical application of the $Ti_3C_2T_x$ MXene−matrigel hydrogel to promote the recovery of SGNs, thereby optimizing the postoperative listening effect of cochlear implantation.

CONCLUSION

In summary, our findings demonstrated that the $Ti_3C_2T_x$ MXene−matrigel hydrogel had a certain promoting effect on the growth of SGNs compared with matrigel hydrogel alone. $Ti_3C_2T_x$ MXene−matrigel hydrogel exhibited great cytocompatibility and was an excellent interface material for SGNs. What's more, the introduction of a 3D low-frequency cochlear implant−$Ti_3C_2T_x$ MXene−matrigel hydrogel−EAS system could further enhance the regulatory effect on SGN growth and neural network formation *in vitro*. This system may have potential application for the establishment of a comprehensive technical system for cochlear implantation and SGNs repair. This will expand the scope of application of CI, and help more patients with sensorineural hearing loss to recover or increase hearing perception.

METHODS

Animals. The mice used in the experiments were approved by the Animal Care and Use Committee of Southeast University and agree with the National Institutes of Health Guide for the Care and Use of Laboratory Animals. The wild-type (WT) mice used were the FVB strain.

Preparation of $Ti_3C_2T_x$ MXene and Hydrogels. The hydrothermal reaction kettle was cleaned with a NaOH solution and deionized water. LiF (1 g), deionized water, and HCl (10 mL) were added to the dried hydrothermal reaction kettle, and the mixture was stirred with a magnetic stirrer. Then, to the mixture was slowly added MAX (1 g). After the hydrothermal reaction kettle was wrapped with plastic wrap, it was placed in a water bath (40 °C), and the mixture was stirred continuously for at least 24 h. The next day, the liquid in the hydrothermal reaction kettle was transferred to centrifuge tubes and centrifuged at 3500 rpm for 10 min. The supernatant was discarded, and the precipitant was shaken to resuspend it with deionized water and centrifuged again. After each centrifugation, the speed was increased by 500 rpm until the final centrifugation speed of 7500 rpm. Finally, the $Ti_3C_2T_x$ MXene solution was obtained after resuspension with deionized water. Concentration determination and TEM detection were then performed.

The night before the experiment, the matrigel (CORNING, 354234) was fully thawed in an ice box placed in a 4 °C freezer. The matrigel, UV-sterilized $Ti_3C_2T_x$ MXene, extracted SGNs, and the culture medium (or water, when used for characterization) were mixed and prepared into precursor solutions of $Ti_3C_2T_x$ MXene at different concentrations, with the matrigel accounting for 70%. The solution was mixed gently to avoid air bubbles, then t a volume of the precursor solution was transferred to a Petri dish or mold and placed in an incubator at 37 °C for 3−5 min. Subsequently, the Petri dish was inverted for 2−3 min to allow it to solidify uniformly and form a stable hydrogel.

Characterization of $Ti_3C_2T_x$ MXene and the $Ti_3C_2T_x$ MXene−matrigel Hydrogel. The morphologies of $Ti_3C_2T_x$ MXene nanosheets were observed by TEM (JEM-2100). The Raman spectra of $Ti_3C_2T_x$ MXene were obtained with a Raman microscope (HORIBA Scientific, LabRAM HR Evolution, France), and the surface chemical pattern was obtained on an X-ray photoelectron spectrometer (XPS, Thermo Fisher Scientific, Nexsa, USA). Stability studies were performed using SEM−EDX and UV−vis measurements of aqueous $Ti_3C_2T_x$ MXene, which were performed on a UV−vis spectrophotometer (BioTek, CYTATION5 imaging reader).[36,44] For UV−vis measurements, 100 μL aliquots of the aqueous solution of $Ti_3C_2T_x$ MXene in eppendorf tubes were stored in a laboratory drawer or a 4 °C refrigerator in a dark environment for 30 days. One tube was taken and vortexed for each measurement and then diluted to a concentration of 300 μg/mL. The absorbance value at 785 nm was used to quantify the change in $Ti_3C_2T_x$ MXene over time. The porous structure of the $Ti_3C_2T_x$ MXene hydrogel was observed through SEM (SEM, Zeiss, Ultra Plus, Germany). The hydrogels were analyzed using SEM coupled with EDX to confirm that the $Ti_3C_2T_x$ MXene nanosheets were successfully integrated into the matrigel. The equilibrium swelling ratio (ESR) of the $Ti_3C_2T_x$ MXene−matrigel hydrogel was calculated using the following formula: $ESR = (W_s - W_d)/(W_t - W_d)$, where W_s is the weight of the hydrogel after swelling equilibrium, W_d is the dry weight of the gel, and W_t is the initial weight of the gel.

https://doi.org/10.1021/acsnano.2c06306
ACS Nano 2022, 16, 16744−16756

Culture of Spiral Ganglion Neurons. DMEM/F12 medium (Gibco, 11330−0032), 10% fetal bovine serum (Pansera, P30-3302) and 50 μg/mL ampicillin formed the day 1 culture medium (SGN1). Growth factors, including B27, N2, 10 ng/mL FGF, 20 ng/mL EGF, and 50 ng/mL IGF, were added to the DMEM/F12 medium to prepare the complete medium (SGN2) required for SGNs. The P2−P3 (P = postnatal) wild-type mice were first subjected to freezing anesthesia. After being treated with alcohol, the temporal bones were dissected under a stereomicroscope in HBSS (Gibco, C14175500BT). The organ of Corti was then removed, and the modiolus was transferred to PBS (Sigma, P5493). After collection, the modiolus was digested with preheated 0.125% trypsin (Gibco, 15050065) in a 37 °C incubator for 8 to 10 min. After the digestion solution was changed to the culture medium, the modiolus was gently pipetted several times to dissociate the tissue, then filtered to obtain a single-cell suspension. $Ti_3C_2T_x$ MXene and cells were mixed into matrigel to make a certain concentration of hydrogel, and the proportion of matrigel was 70%. After the hydrogels were solidified, the SGN1 medium was added, and the samples were then placed in a 37 °C incubator with a carbon dioxide concentration of 5%. The next day, the SGN1 medium was replaced with the SGN2 medium. The SGN2 medium was changed every two days.

Cytotoxicity Test. For Calcein-AM/EthD-1 staining, 4 mM Calcein-AM (Thermo Fisher Scientific, c3099) and 2 mM Ethd-1 were diluted with DMEM/F12 to final concentrations of 2 and 0.5 μM, respectively. The medium was removed, and the cells were washed with PBS and incubated with a prepared Calcein-AM/EthD-1 solution above at 37 °C for 30 min in the dark. Then the cells were washed three times with PBS for 5 min each time and observed and captured by a laser scanning confocal microscope.

For the Cell Counting Kit-8 (CCK-8) assay, the medium and CCK-8 (Beyotime, C0039) reagent were prepared in a ratio of 10:1. The medium was removed, and the cells were washed with PBS and incubated with diluted CCK-8 solution at 37 °C for 2 h in the dark. After the incubation, the reacted solution was transferred to another 96-well plate, and the absorbance was measured at 450 nm.

Real-Time Quantitative PCR (RT-qPCR). The cell recovery solution (CORNING, 354253) was used to separate the cells from the $Ti_3C_2T_x$ MXene−matrigel hydrogel. Cells were then incubated on ice for 20−30 min. After centrifugation, the cells with 1 mL of Trizol were left standing on ice for 10 min until they were fully lysed. Centrifugation was then performed at 14 000 *g* for 15 min. The supernatant was carefully taken out, and chloroform (0.2 mL) was added to the samples. The samples were then mixed well, placed on ice for 5 min, and centrifuged again at 14 000 *g* for 15 min. Subsequently, the upper aqueous phase containing RNA was carefully gathered. An equal volume of isopropanol was added, and the samples were placed on ice for 10 min and then centrifuged at 14 000 *g* for 10 min. To wash the sediment, 1 mL of 75% ethanol (prepared with DEPC water) was used. After the sample was centrifuged at 7500 *g* for 5 min, DEPC water (50 μL) was added to solubilize the RNA. The above operations are all carried out at a low temperature. The mRNA was reverse transcribed into cDNA by using a cDNA synthesis kit (Thermo Fisher Scientific, K1622). The reverse transcription reaction was performed at 42 °C for 1 h, then at 95 °C for 5 min. RT-qPCR was performed with SYBR Green Master (Roche, 04913914001). The comparative cycle threshold ($2^{-\Delta\Delta C_t}$) method was used to analyze the data.

Immunofluorescence. The samples were fixed with 4% paraformaldehyde (PFA) for 1 h at room temperature (RT) and then permeabilized with 0.1% PBST (0.1 M PBS with 0.01% Triton X-100). Specifically, for PSD95 staining, the samples should be incubated with 0.1× pepsin (DAKO, S3002) for 3−5 min for antigenic repair. This step was not necessary for other antigen stains. The cells were blocked with a blocking solution for 1 h at RT, then the solution was replaced with the corresponding primary antibody at 4 °C overnight. The primary antibodies used in this work are as follows: anti-PSD95 (Millipore, MAB1596), anti-Tuj1 antibody (Abcam, ab78078), and anti-Synapsin-1 antibody (Cell Signaling Technology, 5297T). The cells were washed three times with 0.1% PBST and then incubated with the corresponding secondary antibodies and DAPI for 1 h at RT. The secondary antibodies included donkey antirabbit 555 (Invitrogen, A31572), donkey antimouse 555 (Invitrogen, A31570), goat antimouse IgG2a 488 (Invitrogen, A21131), and Alexa fluor 488 phalloidin (Thermo Fisher Scientific, A12379). Finally, the antifluorescence quencher DAKO (DAKO, S3023) was used to cover the slides. A Zeiss LSM900 confocal microscope was used to observe and capture images.

Scanning Electron Microscope. For cell samples, 2.5% glutaraldehyde was used to fix the cells overnight at 4 °C. After being washed four times with PBS on ice, the samples with PBS were placed in a −80 °C refrigerator for freezing. For different hydrogels, deionized water was directly added for freezing. Then, a vacuum desiccator was used to dry the cells and hydrogels. Before imaging, the samples should be fixed on the SEM sample holder with conductive tape and sprayed gold for five or six times. Finally, the samples were scanned in the high-vacuum mode for observation and imaging.

Calcium Imaging. The F-127 solution and Flou4-AM (Thermo Fisher Scientific, F14201) were mixed in equal volumes to prepare a working stock solution. The stock solution was diluted to a working concentration with phenol red-free DMEM/F12 medium (Thermo Fisher Scientific, 11039021). The diluted working solution was then added to cell samples, and samples were incubated in dark for 10−15 min. After being washed three times with PBS, the samples were placed in phenol red-free DMEM/F12 medium for further imaging. The processed samples were observed with the 20× or 40× water immersion objective of a two-photon microscope (Zeiss, LSM-710). Images were taken every 600 ms in the time series mode, and a total of 500 images were continuously collected in one field of view. The resolution was selected as 512 × 512. The ROI of each cell and the change of background fluorescence intensity over time were directly extracted with ImageJ software. The standard fluorescence intensity (ΔF) is the ROI fluorescence intensity divided by the background fluorescence intensity.

Electroacoustic Stimulation of SGNs in $Ti_3C_2T_x$ MXene−Matrigel Hydrogel. The cochlear implant electroacoustic stimulation system was constructed as previously described.[38,45] Briefly, the $Ti_3C_2T_x$ MXene hydrogel served as the corresponding reference electrode and matrix for the cell culture. The transmission of electrical signals was accomplished by placing the cochlear implant on a printed circuit board (PCB). The reference electrode and 22 full-frequency bands on the PCB can be connected to electrode of the CI. Signals were then transmitted from PCB to the platinum electrodes in the cell culture system on the other side. Thus, the sound was converted into EAS.

Data Processing and Statistics. All experiments were performed in three or more biological replicates. Cytomorphological indicators were measured by ImageJ. Graphing and analysis were done through GraphPad Prism 6 and Microsoft Excel. Statistical analysis was carried out using two-tailed unpaired Student's *t* test and one-way ANOVA. Significant differences were considered when $p < 0.05$. All data are expressed as mean ± SD. Figures were combined in Adobe Illustrator CS6 software.

ASSOCIATED CONTENT

Supporting Information

The Supporting Information is available free of charge at https://pubs.acs.org/doi/10.1021/acsnano.2c06306.

Stability of the $Ti_3C_2T_x$ MXene nanosheet, integration of the $Ti_3C_2T_x$ MXene and the matrigel, and biocompatibility of the $Ti_3C_2T_x$ MXene−matrigel hydrogel (PDF)

AUTHOR INFORMATION

Corresponding Authors

Renjie Chai − *State Key Laboratory of Bioelectronics, Department of Otolaryngology Head and Neck Surgery,*

https://doi.org/10.1021/acsnano.2c06306
ACS Nano 2022, 16, 16744−16756

Zhongda Hospital, School of Life Sciences and Technology, Advanced Institute for Life and Health, Jiangsu Province High-Tech Key Laboratory for Bio-Medical Research, Southeast University, Nanjing, Jiangsu 210096, China; Co-Innovation Center of Neuroregeneration, Nantong University, Nantong, Jiangsu 226001, China; Department of Otolaryngology—Head and Neck Surgery, Sichuan Provincial People's Hospital, University of Electronic Science and Technology of China, Chengdu, Sichuan 610072, China; Institute for Stem Cell and Regeneration, Chinese Academy of Science, Beijing 100101, China; Beijing Key Laboratory of Neural Regeneration and Repair, Capital Medical University, Beijing 100069, China; orcid.org/0000-0002-3885-543X; Email: renjiec@seu.edu.cn

Xia Gao − *Department of Otorhinolaryngology—Head and Neck Surgery, Affiliated Drum Tower Hospital of Nanjing University Medical School, Nanjing, Jiangsu 210008, China*; Email: xiagaogao@hotmail.com

Shan Sun − *ENT Institute, Fudan University, Shanghai 200031, China;* orcid.org/0000-0003-2142-4307; Email: Shansun@fudan.edu.cn

Mingliang Tang − *State Key Laboratory of Bioelectronics, Department of Otolaryngology Head and Neck Surgery, Zhongda Hospital, School of Life Sciences and Technology, Advanced Institute for Life and Health, Jiangsu Province High-Tech Key Laboratory for Bio-Medical Research, Southeast University, Nanjing, Jiangsu 210096, China; Institute for Cardiovascular Science, Soochow University, Suzhou, Jiangsu 215000, China; Co-Innovation Center of Neuroregeneration, Nantong University, Nantong, Jiangsu 226001, China;* orcid.org/0000-0003-4215-123X; Email: mltang@suda.edu.cn

Authors

Menghui Liao − *State Key Laboratory of Bioelectronics, Department of Otolaryngology Head and Neck Surgery, Zhongda Hospital, School of Life Sciences and Technology, Advanced Institute for Life and Health, Jiangsu Province High-Tech Key Laboratory for Bio-Medical Research, Southeast University, Nanjing, Jiangsu 210096, China; Department of Otorhinolaryngology—Head and Neck Surgery, Affiliated Drum Tower Hospital of Nanjing University Medical School, Nanjing, Jiangsu 210008, China*

Yangnan Hu − *State Key Laboratory of Bioelectronics, Department of Otolaryngology Head and Neck Surgery, Zhongda Hospital, School of Life Sciences and Technology, Advanced Institute for Life and Health, Jiangsu Province High-Tech Key Laboratory for Bio-Medical Research, Southeast University, Nanjing, Jiangsu 210096, China; Department of Otorhinolaryngology—Head and Neck Surgery, Affiliated Drum Tower Hospital of Nanjing University Medical School, Nanjing, Jiangsu 210008, China*

Yuhua Zhang − *State Key Laboratory of Bioelectronics, Department of Otolaryngology Head and Neck Surgery, Zhongda Hospital, School of Life Sciences and Technology, Advanced Institute for Life and Health, Jiangsu Province High-Tech Key Laboratory for Bio-Medical Research, Southeast University, Nanjing, Jiangsu 210096, China*

Kaichen Wang − *Chien-Shiung Wu College, Southeast University, Nanjing, Jiangsu 210096, China*

Qiaojun Fang − *State Key Laboratory of Bioelectronics, Department of Otolaryngology Head and Neck Surgery, Zhongda Hospital, School of Life Sciences and Technology, Advanced Institute for Life and Health, Jiangsu Province High-Tech Key Laboratory for Bio-Medical Research, Southeast University, Nanjing, Jiangsu 210096, China*

Yanru Qi − *State Key Laboratory of Bioelectronics, Department of Otolaryngology Head and Neck Surgery, Zhongda Hospital, School of Life Sciences and Technology, Advanced Institute for Life and Health, Jiangsu Province High-Tech Key Laboratory for Bio-Medical Research, Southeast University, Nanjing, Jiangsu 210096, China*

Yingbo Shen − *Chien-Shiung Wu College, Southeast University, Nanjing, Jiangsu 210096, China*

Hong Cheng − *State Key Laboratory of Bioelectronics, Department of Otolaryngology Head and Neck Surgery, Zhongda Hospital, School of Life Sciences and Technology, Advanced Institute for Life and Health, Jiangsu Province High-Tech Key Laboratory for Bio-Medical Research, Southeast University, Nanjing, Jiangsu 210096, China*

Xiaolong Fu − *State Key Laboratory of Bioelectronics, Department of Otolaryngology Head and Neck Surgery, Zhongda Hospital, School of Life Sciences and Technology, Advanced Institute for Life and Health, Jiangsu Province High-Tech Key Laboratory for Bio-Medical Research, Southeast University, Nanjing, Jiangsu 210096, China*

Complete contact information is available at: https://pubs.acs.org/10.1021/acsnano.2c06306

Author Contributions

M.L. and Y.H. contributed equally to this paper. M.L. and YH. designed and performed experiments and drafted the manuscript; Y.Z. and Q.F. provided technical suggestions; Y.Q. and H.C. helped with data processing; X.F. helped with performing the experiments; K.W., M.L., Y.H., and Y.S. revised the manuscript; R.C., X.G., S.S., and M.T. conceived of the project, provided supervision, acquired funding, and edited the manuscript.

Notes

The authors declare no competing financial interest.

ACKNOWLEDGMENTS

This work was supported by grants from National Key R&D Program of China (Grants 2021YFA1101300 and 2020YFA0112503); the Strategic Priority Research Program of the Chinese Academy of Science (Grant XDA16010303); the National Natural Science Foundation of China (Grants 82030029, 81970882, 81970883, and 92149304); the Natural Science Foundation of Jiangsu Province (Grant BE2019711); the Science and Technology Department of Sichuan Province (Grant 2021YFS0371); the Shenzhen Fundamental Research Program (Grants JCYJ20190814093401920 and JCYJ20210324125608022); and the Open Research Fund of State Key Laboratory of Genetic Engineering, Fudan University (Grant SKLGE-2104).

REFERENCES

(1) Ramsden, J. D.; Gordon, K.; Aschendorff, A.; Borucki, L.; Bunne, M.; Burdo, S.; Garabedian, N.; Grolman, W.; Irving, R.; Lesinski-Schiedat, A.; Loundon, N.; Manrique, M.; Martin, J.; Raine, C.; Wouters, J.; Papsin, B. C. European Bilateral Pediatric Cochlear Implant Forum Consensus Statement. *Otol Neurotol.* **2012**, *33*, 561−565.

(2) Loizou, P. C.; Mani, A.; Dorman, M. F. Dichotic Speech Recognition in Noise Using Reduced Spectral Cues. *J. Acoust Soc. Am.* **2003**, *114*, 475−483.

(3) Brigande, J. V.; Heller, S. Quo Vadis, Hair Cell Regeneration? *Nat. Neurosci.* **2009**, *12*, 679−685.
(4) Houston, D. M.; Stewart, J.; Moberly, A.; Hollich, G.; Miyamoto, R. T. Word Learning in Deaf Children with Cochlear Implants: Effects of Early Auditory Experience. *Dev Sci.* **2012**, *15*, 448−461.
(5) Wise, A. K.; Pujol, R.; Landry, T. G.; Fallon, J. B.; Shepherd, R. K. Structural and Ultrastructural Changes to Type I Spiral Ganglion Neurons and Schwann Cells in the Deafened Guinea Pig Cochlea. *J. Assoc Res. Otolaryngol.* **2017**, *18*, 751−769.
(6) Shepherd, R. K.; Coco, A.; Epp, S. B. Neurotrophins and Electrical Stimulation for Protection and Repair of Spiral Ganglion Neurons Following Sensorineural Hearing Loss. *Hear Res.* **2008**, *242*, 100−109.
(7) Zheng, F.; Zuo, J. Cochlear Hair Cell Regeneration after Noise-Induced Hearing Loss: Does Regeneration Follow Development? *Hear Res.* **2017**, *349*, 182−196.
(8) Chen, Y.; Gu, Y.; Li, Y.; Li, G. L.; Chai, R.; Li, W.; Li, H. Generation of Mature and Functional Hair Cells by Co-Expression of Gfi1, Pou4f3, and Atoh1 in the Postnatal Mouse Cochlea. *Cell Rep.* **2021**, *35*, 109016.
(9) Spitzer, N. C. Electrical Activity in Early Neuronal Development. *Nature* **2006**, *444*, 707−712.
(10) Zhang, Z.; Rouabhia, M.; Wang, Z.; Roberge, C.; Shi, G.; Roche, P.; Li, J.; Dao, L. H. Electrically Conductive Biodegradable Polymer Composite for Nerve Regeneration: Electricity-Stimulated Neurite Outgrowth and Axon Regeneration. *Artif Organs.* **2007**, *31*, 13−22.
(11) Ghasemi-Mobarakeh, L.; Prabhakaran, M. P.; Morshed, M.; Nasr-Esfahani, M. H.; Ramakrishna, S. Electrical Stimulation of Nerve Cells Using Conductive Nanofibrous Scaffolds for Nerve Tissue Engineering. *Tissue Eng. Part A* **2009**, *15*, 3605−3619.
(12) Kopelovich, J. C.; Cagaanan, A. P.; Miller, C. A.; Abbas, P. J.; Green, S. H. Intracochlear Electrical Stimulation Suppresses Apoptotic Signaling in Rat Spiral Ganglion Neurons after Deafening in Vivo. *Otolaryngol Head Neck Surg* **2013**, *149*, 745−752.
(13) Gordon, T.; Amirjani, N.; Edwards, D. C.; Chan, K. M. Brief Post-Surgical Electrical Stimulation Accelerates Axon Regeneration and Muscle Reinnervation without Affecting the Functional Measures in Carpal Tunnel Syndrome Patients. *Exp. Neurol.* **2010**, *223*, 192−202.
(14) Latchoumane, C. V.; Jackson, L.; Sendi, M. S. E.; Tehrani, K. F.; Mortensen, L. J.; Stice, S. L.; Ghovanloo, M.; Karumbaiah, L. Chronic Electrical Stimulation Promotes the Excitability and Plasticity of Esc-Derived Neurons Following Glutamate-Induced Inhibition In Vitro. *Sci. Rep.* **2018**, *8*, 10957.
(15) Shen, N.; Liang, Q.; Liu, Y.; Lai, B.; Li, W.; Wang, Z.; Li, S. Charge-Balanced Biphasic Electrical Stimulation Inhibits Neurite Extension of Spiral Ganglion Neurons. *Neurosci. Lett.* **2016**, *624*, 92−99.
(16) Seo, H.; Jun, S. C. Relation between the Electric Field and Activation of Cortical Neurons in Transcranial Electrical Stimulation. *Brain Stimul* **2019**, *12*, 275−289.
(17) Lafon, B.; Rahman, A.; Bikson, M.; Parra, L. C. Direct Current Stimulation Alters Neuronal Input/Output Function. *Brain Stimulation* **2017**, *10*, 36−45.
(18) Yim, E. K.; Darling, E. M.; Kulangara, K.; Guilak, F.; Leong, K. W. Nanotopography-Induced Changes in Focal Adhesions, Cytoskeletal Organization, and Mechanical Properties of Human Mesenchymal Stem Cells. *Biomaterials* **2010**, *31*, 1299−1306.
(19) Tilghman, R. W.; Parsons, J. T. Focal Adhesion Kinase as a Regulator of Cell Tension in the Progression of Cancer. *Semin Cancer Biol.* **2008**, *18*, 45−52.
(20) Naguib, M.; Kurtoglu, M.; Presser, V.; Lu, J.; Niu, J.; Heon, M.; Hultman, L.; Gogotsi, Y.; Barsoum, M. W. Two-Dimensional Nanocrystals Produced by Exfoliation of Ti3 Alc2. *Adv. Mater.* **2011**, *23*, 4248−4253.
(21) Byeon, A.; Zhao, M. Q.; Ren, C. E.; Halim, J.; Kota, S.; Urbankowski, P.; Anasori, B.; Barsoum, M. W.; Gogotsi, Y. Two-Dimensional Titanium Carbide Mxene as a Cathode Material for Hybrid Magnesium/Lithium-Ion Batteries. *ACS Appl. Mater. Interfaces.* **2017**, *9*, 4296−4300.
(22) Naguib, M.; Mochalin, V. N.; Barsoum, M. W.; Gogotsi, Y. 25th Anniversary Article: Mxenes: A New Family of Two-Dimensional Materials. *Adv. Mater.* **2014**, *26*, 992−1005.
(23) Ghidiu, M.; Lukatskaya, M. R.; Zhao, M. Q.; Gogotsi, Y.; Barsoum, M. W. Conductive Two-Dimensional Titanium Carbide 'Clay' with High Volumetric Capacitance. *Nature* **2014**, *516*, 78−81.
(24) Yoon, J.; Shin, M.; Lim, J.; Lee, J. Y.; Choi, J. W. Recent Advances in Mxene Nanocomposite-Based Biosensors. *Biosensors (Basel)* **2020**, *10*, 185.
(25) Kamysbayev, V.; Filatov, A. S.; Hu, H.; Rui, X.; Lagunas, F.; Wang, D.; Klie, R. F.; Talapin, D. V. Covalent Surface Modifications and Superconductivity of Two-Dimensional Metal Carbide Mxenes. *Science* **2020**, *369*, 979−983.
(26) Chen, K.; Qiu, N.; Deng, Q.; Kang, M. H.; Yang, H.; Baek, J. U.; Koh, Y. H.; Du, S.; Huang, Q.; Kim, H. E. Cytocompatibility of Ti3alc2, Ti3sic2, and Ti2aln: In Vitro Tests and First-Principles Calculations. *ACS Biomater Sci. Eng.* **2017**, *3*, 2293−2301.
(27) Wu, L.; Lu, X.; Dhanjai; Wu, Z. S.; Dong, Y.; Wang, X.; Zheng, S.; Chen, J. 2d Transition Metal Carbide Mxene as a Robust Biosensing Platform for Enzyme Immobilization and Ultrasensitive Detection of Phenol. *Biosens Bioelectron* **2018**, *107*, 69−75.
(28) Yu, X.; Cai, X.; Cui, H.; Lee, S. W.; Yu, X. F.; Liu, B. Fluorine-Free Preparation of Titanium Carbide Mxene Quantum Dots with High near-Infrared Photothermal Performances for Cancer Therapy. *Nanoscale* **2017**, *9*, 17859−17864.
(29) Dai, C.; Chen, Y.; Jing, X.; Xiang, L.; Yang, D.; Lin, H.; Liu, Z.; Han, X.; Wu, R. Two-Dimensional Tantalum Carbide (Mxenes) Composite Nanosheets for Multiple Imaging-Guided Photothermal Tumor Ablation. *ACS Nano* **2017**, *11*, 12696−12712.
(30) Gao, Y.; Dong, Y.; Yang, S.; Mo, A.; Zeng, X.; Chen, Q.; Peng, Q. Size-Dependent Photothermal Antibacterial Activity of Ti3c2tx Mxene Nanosheets against Methicillin-Resistant Staphylococcus Aureus. *J. Colloid Interface Sci.* **2022**, *617*, 533−541.
(31) Liu, S.; Zeng, T. H.; Hofmann, M.; Burcombe, E.; Wei, J.; Jiang, R.; Kong, J.; Chen, Y. Antibacterial Activity of Graphite, Graphite Oxide, Graphene Oxide, and Reduced Graphene Oxide: Membrane and Oxidative Stress. *ACS Nano* **2011**, *5*, 6971−6980.
(32) Li, Z.; Zhang, H.; Han, J.; Chen, Y.; Lin, H.; Yang, T. Surface Nanopore Engineering of 2D Mxenes for Targeted and Synergistic Multitherapies of Hepatocellular Carcinoma. *Adv. Mater.* **2019**, *31*, e1902282.
(33) Guo, R.; Xiao, M.; Zhao, W.; Zhou, S.; Hu, Y.; Liao, M.; Wang, S.; Yang, X.; Chai, R.; Tang, M. 2d Ti3c2txmxene Couples Electrical Stimulation to Promote Proliferation and Neural Differentiation of Neural Stem Cells. *Acta Biomater* **2022**, *139*, 105−117.
(34) Kleinman, H. K.; Martin, G. R. Matrigel: Basement Membrane Matrix with Biological Activity. *Semin Cancer Biol.* **2005**, *15*, 378−386.
(35) Rackham, C. L.; Jones, P. M.; King, A. J. Maintenance of Islet Morphology Is Beneficial for Transplantation Outcome in Diabetic Mice. *PLoS One* **2013**, *8*, e57844.
(36) Shuck, C. E.; Han, M. K.; Maleski, K.; Hantanasirisakul, K.; Kim, S. J.; Choi, J.; Reil, W. E. B.; Gogotsi, Y. Effect of Ti3alc2Max Phase on Structure and Properties of Resultant Ti3c2tx Mxene. *Acs Appl. Nano Mater.* **2019**, *2*, 3368−3376.
(37) Berthiaume, F.; Maguire, T. J.; Yarmush, M. L. Tissue Engineering and Regenerative Medicine: History, Progress, and Challenges. *Annu. Rev. Chem. Biomol Eng.* **2011**, *2*, 403−430.
(38) Guo, R.; Liao, M.; Ma, X.; Hu, Y.; Qian, X.; Xiao, M.; Gao, X.; Chai, R.; Tang, M. Cochlear Implant-Based Electric-Acoustic Stimulation Modulates Neural Stem Cell-Derived Neural Regeneration. *J. Mater. Chem. B* **2021**, *9*, 7793−7804.
(39) Li, X.; Macewan, M. R.; Xie, J. D.; Siewe, D.; Yuan, X.; Xia, Y. Fabrication of Density Gradients of Biodegradable Polymer Microparticles and Their Use in Guiding Neurite Outgrowth. *Adv. Funct Mater.* **2010**, *20*, 1632−1637.

https://doi.org/10.1021/acsnano.2c06306
ACS Nano 2022, 16, 16744−16756

(40) Meyer, D.; Bonhoeffer, T.; Scheuss, V. Balance and Stability of Synaptic Structures During Synaptic Plasticity. *Neuron* **2014**, *82*, 430−443.
(41) Ohn, T. L.; Rutherford, M. A.; Jing, Z. Z.; Jung, S. Y.; Duque-Afonso, C. J.; Hoch, G.; Picher, M. M.; Scharinger, A.; Strenzke, N.; Moser, T. Hair Cells Use Active Zones with Different Voltage Dependence of Ca^{2+} Influx to Decompose Sounds into Complementary Neural Codes. *P Natl. Acad. Sci. U.S.A.* **2016**, *113*, E4716−E4725.
(42) Wong, A. B.; Rutherford, M. A.; Gabrielaitis, M.; Pangršič, T.; Göttfert, F.; Frank, T.; Michanski, S.; Hell, S.; Wolf, F.; Wichmann, C.; Moser, T. Developmental Refinement of Hair Cell Synapses Tightens the Coupling of Ca^{2+} Influx to Exocytosis. *EMBO J.* **2014**, *33* (3), 247−264.
(43) Xiao, M.; Li, X.; Song, Q.; Zhang, Q.; Lazzarino, M.; Cheng, G.; Ulloa Severino, F. P.; Torre, V. A Fully 3D Interconnected Graphene-Carbon Nanotube Web Allows the Study of Glioma Infiltration in Bioengineered 3D Cortex-Like Networks. *Adv. Mater.* **2018**, *30*, 1806132.
(44) Zhang, C. F. J.; Pinilla, S.; McEvoy, N.; Cullen, C. P.; Anasori, B.; Long, E.; Park, S. H.; Seral-Ascaso, A.; Shmeliov, A.; Krishnan, D.; Morant, C.; Liu, X. H.; Duesberg, G. S.; Gogotsi, Y.; Nicolosi, V. Oxidation Stability of Colloidal Two-Dimensional Titanium Carbides (MXenes). *Chem. Mater.* **2017**, *29*, 4848−4856.
(45) Guo, R.; Ma, X.; Liao, M.; Liu, Y.; Hu, Y.; Qian, X.; Tang, Q.; Guo, X.; Chai, R.; Gao, X.; Tang, M. Development and Application of Cochlear Implant-Based Electric-Acoustic Stimulation of Spiral Ganglion Neurons. *ACS Biomater Sci. Eng.* **2019**, *5*, 6735−6741.

https://doi.org/10.1021/acsnano.2c06306
ACS Nano 2022, 16, 16744−16756